THE ASTROPHYSICAL JOURNAL, 470:961–966, 1996 October 20

ASCA OBSERVATIONS OF THE COMPOSITE SUPERNOVA REMNANT G29.7−0.3

ELIZABETH L. BLANTON AND DAVID J. HELFAND
Department of Astronomy, Columbia University, New York, NY 10027
Received 1995 December 28; accepted 1996 May 10

ABSTRACT

We confirm the composite nature of the supernova remnant (SNR) G29.7−0.3 (Kes 75) using observations in the 0.5–8 keV energy range obtained with the *ASCA* X-ray observatory. Spatial and spectral analyses of the data show that G29.7−0.3 is composed of a hard X-ray, nonthermal central source and a soft X-ray, thermal shell. Combining the results of our analysis with radio determinations of the distance to G29.7−0.3 and its shell diameter (Becker & Helfand), we estimate the luminosities of the two components of the SNR as well as its total mass and age. The Crab-like core has an X-ray luminosity of $L_X \approx 1 \times 10^{36}$ ergs s^{-1}, making it the second most luminous synchrotron nebula in the Galaxy. The thermal X-ray emission of the shell supports an age estimate comparable to that of the Crab, and the shell's inferred composition and mass are consistent with a massive progenitor. An estimate of the current energy loss rate of the unseen pulsar from the synchrotron nebula's X-ray luminosity, coupled with a calculation of the total energy in nebular particles and fields from the shape of the radio–to–X-ray spectrum, also gives an age estimate of $\approx 10^3$ yr.

Subject headings: ISM: individual (G29.7−0.3) — supernova remnants — X-rays: ISM

1. INTRODUCTION

Supernovae are instructors in nucleosynthesis and stellar evolution. Tracking a supernova shortly after outburst, constructing a light curve, and examining its optical spectrum give insight into the properties of the progenitor star and the abundances of elements ejected during the explosion. Longer after the event, high-resolution X-ray spectroscopy of supernova remnants (SNRs), available for the first time from the *Advanced Satellite for Cosmology and Astrophysics* (*ASCA*), can also be used to assess the abundances of elements ejected during the explosion. In addition, these observations can separate a hard X-ray, compact central source powered by a young neutron star from a soft X-ray, thermal plasma in a surrounding shell. Composite SNRs—incorporating both of these components—are the expected result of the canonical view of a Type II (or Type Ib) supernova explosion. Studying SNRs, then, allows us to test current supernova theory: Type II (or Type Ib) supernovae are the result of the core collapse of a massive star that has expended its supply of nuclear fuel, and their remnants would be expected to include O and its burning products, Ne and Mg, in an expanding shell surrounding a central neutron star; a Type Ia supernova is the result of the explosion of a white dwarf that has surpassed its Chandrasekhar limit by accreting mass from a companion, leaving a remnant rich in Fe, less rich in Mg than a Type II, little O or Ne, and without a compact source at its center. When we examine SNRs, do we see the "correct" association between the elements present and the inclusion, or lack of, a compact central source?

To illustrate our new capability to make such distinctions on observational grounds, we present here *ASCA* observations of the composite SNR G29.7−0.3. Previous observations of this source, in the radio band using the VLA and at X-ray wavelengths with the *Einstein Observatory*, are described by Becker & Helfand (1984) and Becker, Helfand, & Szymkowiak (1983). G29.7−0.3 exhibits properties of both a Crab-like and a shell-type remnant. Typical of a Crab-like SNR, G29.7−0.3 has a central component 30″ across with highly polarized radio emission, a flat radio spectral index, and an X-ray spectrum that can be fitted with a power law. These attributes are due to a strong magnetic field and synchrotron-emitting electrons generated by a compact object. Typical of a shell remnant, G29.7−0.3 also exhibits a limb-brightened shell of radio emission 3′.5 in diameter with a steep radio spectral index. The spatial resolution, spectral resolution, and sensitivity of the *Einstein* observation of this source were not sufficient to show definitively the two different X-ray components expected for such a remnant—thermal, soft X-ray emission from the shell and nonthermal, hard X-ray emission from the Crab-like center—although there was some evidence to suggest both were present. Estimates of X-ray luminosity from the Crab-like core indicated that G29.7−0.3 had the highest L_X of any of the other five Crab-like SNRs known at the time, excepting only the Crab itself (Becker, Helfand, & Szymkowiak 1983).

Although conventional models would predict a large percentage of composite SNRs in the Milky Way, since up to ≈85% of Galactic supernovae are thought to arise from massive stars (Tammann, Loeffler, & Schroeder 1994), only 19 remnants out of the 194 known SNRs in the Galaxy show both shell and Crab-like components (Green 1995). This may be due largely to the inability of instruments used in the past to resolve these separate components, rather than to the physical situations not being what current models predict (although we cannot yet exclude the latter as a possibility). *ASCA*, to be described in § 2, gives us the spatial and spectral resolution we need to identify these different components. In the future we may discover that other SNRs, previously classified as single-component remnants, actually fit into the composite category (cf. Vasisht et al. 1995).

In § 3 we present spatial, spectral, and temporal analyses of the *ASCA* observations of G29.7−0.3. The discussion of the results in § 4 includes the determination of the luminosities of the shell and Crab-like components as well as estimates for the mass and age of the remnant.

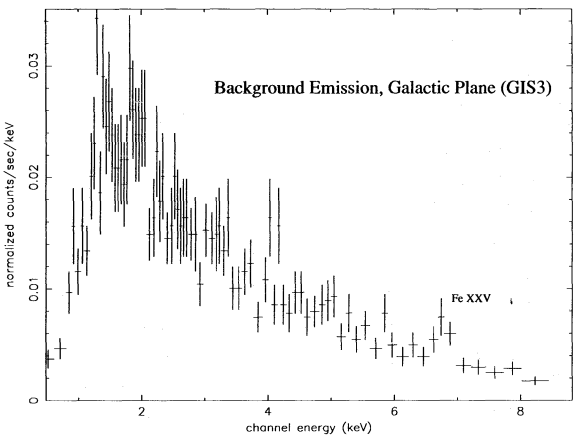

FIG. 1.—GIS3 spectrum of the background emission from the Galactic plane in the region $l = 22.^{\circ}1$–$24.^{\circ}5$, $b = -0.^{\circ}5$ to $+0.^{\circ}5$ folded through the instrument response. The emission line at 6.7 keV is Fe XXV.

2. OBSERVATIONS

Observations were performed with the *ASCA* X-ray satellite (Tanaka, Inoue, & Holt 1994) on 1993 October 12–13 as part of the Performance Verification program; we have extracted these data from the *ASCA* archive at the High Energy Astrophysics Science Archive Research Center (HEASARC) at Goddard Space Flight Center. *ASCA* includes four identical telescopes (XRTs) with thin foil mirrors and focal lengths of 3.5 m providing X-ray images with $\approx 3'$ resolution in the 0.5–12 keV band. An X-ray detector is mounted in the focal plane of each telescope. Two of the detectors are CCD cameras, known as solid state imaging spectrometers (SIS0 and SIS1). Each SIS is made up of four CCD chips and may be used in 1, 2, or 4 CCD mode. The G29.7−0.3 data were taken in 1 CCD mode. The other two detectors are gas scintillation proportional counters or gas imaging spectrometers (GIS2 and GIS3). Compared to the SISs, the GISs have higher quantum efficiency at high energies (94% compared to 47% at 7 keV), better temporal resolution, and 4 times the field of view. The SISs have better energy resolution (2% versus 8% at 5.9 keV for the GISs), greater quantum efficiency at low energies (< 1.5 keV), better angular resolution, and a field of view of $22.^{\prime}8 \times 22.^{\prime}8$ (Tanaka et al. 1994). The strengths and weaknesses of the two types of detectors determine which data we use in the different types of analyses which follow.

The data were cleaned using the data reduction program XSELECT. In the reduction process a number of effects are removed. These include bad aspect (the satellite takes time to settle after making a maneuver), the South Atlantic Anomaly (SAA) (the instruments are not used during a passage through the SAA, but data taken shortly before and after passage still include a high particle background), and Earth occultation (data taken shortly before or after an occultation are not used), among others. Details may be found in the ABC Guide to *ASCA* Data Reduction (1994). After cleaning, 20,711 s of data were obtained with SIS0, 23,207 s with SIS1, 24,826 s with GIS2 and 24,812 s with GIS3.

2.1. *Background Emission*

To correct for background emission, the aforementioned ABC Guide (1994) suggests two approaches. The first is to use a background file obtained during a long exposure of a blank sky region. These files are available via ftp for the SIS and GIS data from a pointing at $b = 90°$. However, the background emission looking out of the plane of the Galaxy is quite different from that found in the plane (our source is at $b = -0.^{\circ}3$). Therefore, these background files were not a good option. The second approach is to use a blank sky region within the field of the source data. Our SIS data were taken in 1 CCD mode which has a small enough field of view ($11.^{\prime}1 \times 11.^{\prime}1$) that a blank area was not available. The GIS data contain a second source in the field, so that a blank area was not available there either. In addition, the responses are not constant over the instruments' fields of view, owing to energy-dependent telescope vignetting as well as detector effects.

Previous X-ray surveys of the Galactic plane (e.g., by *EXOSAT*; Warwick et al. 1985, 1988) have uncovered bright, discrete sources as well as an underlying fainter emission which is apparently diffuse at $\approx 1°$ resolution. Away from the Galactic center, this emission is confined to a width of approximately $b < 1°$ and is called the "Galactic ridge emission." A recent survey with the *Ginga* satellite showed that the 6.7 keV emission line of iron, corresponding to Kα emission from He-like iron (Fe XXV), is a prominent feature in the emission from the Galactic ridge (Yamauchi & Koyama 1993). Fitting the *Ginga* X-ray spectrum with a thermal bremsstrahlung model yields a temperature for the Galactic ridge emission in the range of $(4$–$13) \times 10^7$ K (3.4–11.2 keV). The origin of this emission has not been determined, although it is probably due to an optically thin hot plasma. The plasma may result from either a collection of unresolved faint sources, such as SNRs, or a diffuse process (Yamauchi & Koyama 1993; Warwick et al. 1985, 1988).

In an effort to obtain an accurate background to subtract from our source, we examined sourceless fields near the SNR. We analyzed data obtained in 14 fields from $l = 22.^{\circ}1$ to $l = 24.^{\circ}5$, five at $b = 0.^{\circ}0$, five at $b = +0.^{\circ}5$, and four at $b = -0.^{\circ}5$; these data were collected during *ASCA*'s Galactic plane survey (Helfand 1993). First, we examined the data in the three latitude strips separately: $b = 0.^{\circ}0$ (13,471 s of data), $b = +0.^{\circ}5$ (13,603 s), and $b = -0.^{\circ}5$ (9621 s). After excluding fields containing discrete sources, we were left with a total of 12 fields. The differences in the extracted spectra were small; thus, when producing our final background spectrum, we added all of the fields together and extracted a spectrum in the same region of the detector from which our source spectrum was obtained. The background spectrum for GIS3 with its obvious 6.7 keV Fe XXV line is shown in Figure 1. We caution other *ASCA* observers that errors may result if the *ASCA* $b = 90°$ background file is used to correct for emission from sources in the Galactic plane.

3. ANALYSIS

3.1. *Spatial*

We measure the centroid of the emission from G29.7−0.3 to be located at $\alpha = 18^{h}43^{m}47.^{s}0$ and $\delta = -03°02'28.''8$ (1950). Using the data analysis programs XSELECT and XSPEC to examine *ASCA* SIS data (which have better angular resolution than the GIS data), we determined spectral hardness as a function of radius for G29.7−0.3. We centered progressively larger apertures on the source and determined the count rate in each aperture in two energy

ranges: 0.5–2.5 keV (soft) and 2.5–8.0 keV (hard). The ratio of hard to soft count rates was greatest at the center of the object (within a radius of 60″) and decreased as a function of radius. As a control experiment, we applied the same analysis to a point source, 3C 273, whose hardness we would expect to be constant as a function of radius. Figure 2 shows the definitive contrast between the hardness profiles of the two objects. This, combined with the spectral analysis presented below, clearly illustrates the two-component nature of G29.7−0.3.

In addition, we calculated the flux ratio of the outer region (90″–240″) to the inner region (0″–90″) in narrower energy bands. The ratio is highest in the 1.3–2.0 keV range and declines to its lowest value in the 5.0–8.0 keV range. The values are plotted in Figure 3. This, again, shows that the outer region of the remnant is softer than the inner region and adds flux ratio values for specific energy ranges; line emission from the thin thermal plasma of the shell leads to enhancements in the flux ratio such as that in the 1.3–2.0 keV bin (see § 3.3).

3.2. *Temporal*

Using the GIS data and the XSELECT package, we plotted several light curves. We took different combinations of time-bin sizes and energy bands and searched for fluctuations in the entire source. Long-term fluctuations could be indicative of a variable instrument response or a physical process such as emission from a compact object in a binary star system. The time-bin sizes we selected were 25, 60, and 100 counts bin^{-1}; the energy bands were 0.5–2.5 keV and 2.5–8.0 keV. The time-bin sizes thus constructed range from 112 to 629 s, depending on the number of counts within a particular energy range. We found no significant variability.

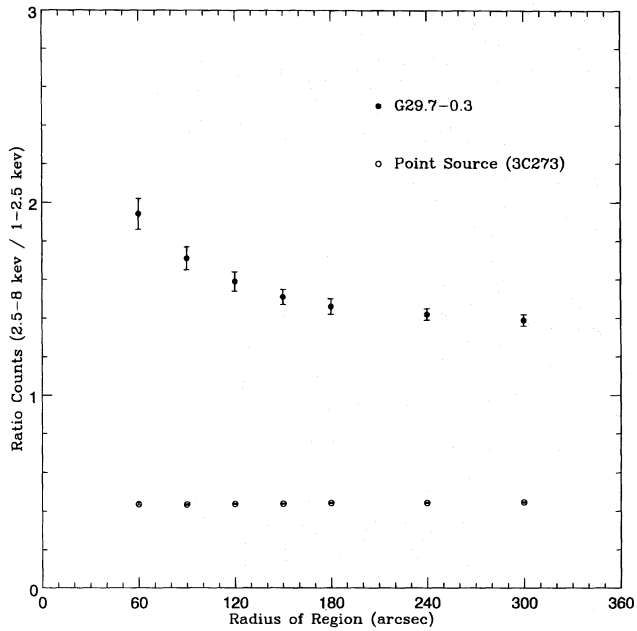

FIG. 2.—Spectral hardness as a function of radius for both G29.7−0.3 and the point source 3C 273. Note that the *x*-axis corresponds to the hardness ratio within a certain radius (i.e., a data point at 120″ corresponds to the ratio of hard to soft counts in the remnant from its center out to 120″). The ratio of hard to soft emission is constant as a function of radius for 3C 273 (as we would expect for a point source), demonstrating that the hardness profile of G29.7−0.3 is not simply due to the mirror point-spread function or response of the instrument. This profile helps confirm that G29.7−0.3 is a composite SNR with hard emission at the center and soft emission in a surrounding shell.

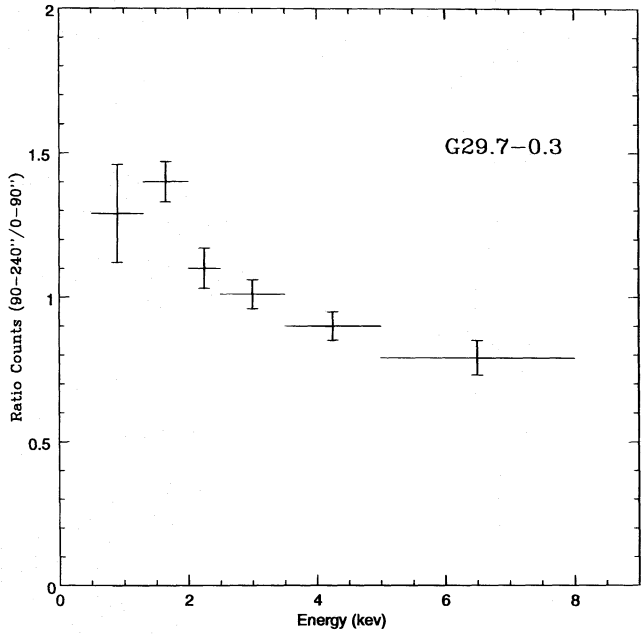

FIG. 3.—Ratio of counts in the outer vs. the inner region of G29.7−0.3 as a function of energy. The ratio is highest in the 1.3–2.0 keV range, in which the Si XIII emission line is prominent, and lowest in the 5–8 keV range, in which the power law dominates. This again shows that the outer region is softer than the interior.

In addition, we searched for periodic variability, such as that which might be expected from a pulsar. We used high bit rate data, which has a resolution of 0.0625 ms, from the GIS3 detector. In order to improve our chances of detecting a period, we attempted to separate flux from the non-thermal, central component from flux from the thermal, softer X-ray shell by extracting photons only from within a 4′ radius of the source center and at energies ≥ 2.5 keV, leaving us with ≈ 3500 counts. We used a combination of the XRONOS fast Fourier transform (FFT) search program PSD and our own software employing the Z^2 statistic (Fierro et al. 1995) to search down to a period of 30 ms. No significant period was found.

3.3. *Spectral*

We extracted spectra using data within an aperture of 300″ centered on the source. A spectrum extracted in this way includes emission from both components of the SNR and so must be fitted with a multicomponent model. As we saw with the spatial analysis, the emission at high energies is dominated by the central component of the SNR. Emission from this component is fitted well with a power-law model, which is indicative of nonthermal emission. The Crab Nebula (pulsar plus synchrotron-emitting plasma), for example, is fitted well with a power law with a photon index of $\Gamma = 2$. To the power-law model we added interstellar absorption and a Raymond-Smith plasma in order to fit the thermal radiation that is dominant at low energies. The Raymond-Smith component is appropriate for a hot, optically thin plasma in ionization equilibrium and with cosmic abundances (Raymond & Smith 1977).

Initially, we simultaneously fitted the three components and achieved values for the column density, temperature, and power-law photon index. In order to estimate the errors on these values, we fixed the photon index at different values, fitted the other components and recorded the varia-

tions in values and in χ^2. Our errors indicate the range of values where the χ^2 remained nearly constant. We performed this fitting process for the four detectors separately and achieved a reduced χ^2 of ≈ 1 for each. For example, the best fit to the SIS1 detector produced a reduced $\chi^2 = 0.9$ (158 for 176 dof). The best-fitting column density, temperature, and photon index are listed for each of the detectors in Table 1. The different detector values agree with each other within 1 σ in most cases; in no case is the discrepancy greater than 2 σ. Fitting the model to the two SISs together gives a power-law photon index of 2.0 ± 0.2, very similar to that of the Crab Nebula, and a plasma temperature of $kT = 0.50 \pm 0.15$ keV ($\chi^2 = 341$ for 352 dof). The absorbing column density of $\approx (3.1 \pm 0.3) \times 10^{22}$ cm^{-2} is a factor of ≈ 1.5 above the measured 21 cm column density of H I to the source (Becker & Helfand 1984), consistent with the expected additional contributions to the absorption from molecular and ionized gas along the line of sight. This agreement is an independent constraint on our spectral fits and lends additional credence to our derived model parameters. Figure 4 shows this model fitted to spectra taken with the SIS0 (*top panel*) and GIS3 (*bottom panel*).

Another fit (Fig. 5) was performed by freezing the power-law photon index with the value we achieved in the above fit ($\Gamma = 2.0$) and varying the following components: absorption, thermal bremsstrahlung emission temperature, and Gaussians at the positions of the three strongest emission lines. The best-fit values determined from the SIS are listed in Table 2. We also include the results from Becker, Helfand, & Szymkowiak (1983) using *Einstein* data, which, within their large uncertainties, are consistent with the *ASCA* results. The positions of the Gaussians correspond to the energies expected for the ions Mg XI, Si XIII, and S XV; measured central energies and equivalent widths are also listed in Table 2. The bottom panel of Figure 5 shows the data compared to the above model with the power-law component omitted. The equivalent widths are defined as the area under the Gaussians divided by the thermal continuum *only* at that position (excluding the nonthermal, power-law continuum, which is from an unrelated emission component). While the line energies agree to within 10 eV, well within their measured uncertainties, there is a significant disagreement between the SIS0 and SIS1 data in determining the line equivalent widths. This is due largely to the different values for the temperature and the contribution of the thermal continuum determined for the spectra from the two detectors. In Table 2 we show parenthetically the equivalent widths that we measured for the lines in the spectrum from the SIS1 data when we adopted the temperature and photon index from the SIS0.

Unfortunately, because of the high column density toward the source and the subsequent absorption of flux at

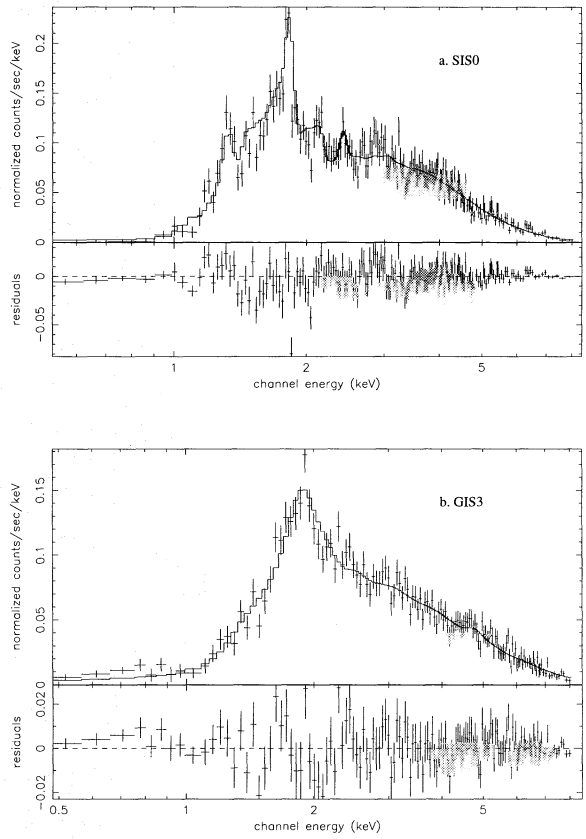

FIG. 4.—(*a*) Spectrum of the *ASCA* SIS0 data for G29.7−0.3. The data have been binned so that one point represents a minimum of 20 counts. The line through the data points is the fit of a model including a Raymond-Smith plasma (thermal bremsstrahlung emission and permitted, semi-forbidden, and forbidden line emission), interstellar absorption, and a power-law component. (*b*) Spectrum of the *ASCA* GIS3 data for G29.7−0.3 binned to a minimum of 20 counts bin^{-1}. The best fit of the model described above to the GIS3 data gives results consistent with the SIS fit (see Table 1).

TABLE 1

BEST FIT WITH RS PLASMA, POWER LAW, AND INTERSTELLAR ABSORPTION

Instrument	Photon Index	kT (keV)	N_H ($\times 10^{22}$ cm^{-2})
SIS0	2.0 ± 0.2	0.45 ± 0.15	3.3 ± 0.3
SIS1	1.9 ± 0.2	0.60 ± 0.15	2.7 ± 0.3
GIS2	2.0 ± 0.2	0.35 ± 0.15	3.8 ± 0.5
GIS3	2.1 ± 0.2	0.45 ± 0.15	3.4 ± 0.5

TABLE 2

BEST FIT WITH THERMAL BREMSSTRAHLUNG, GAUSSIANS, POWER LAW, AND INTERSTELLAR ABSORPTION

Parameter	SIS0	SIS1	*Einstein*
kT (keV)	0.79 ± 0.63	0.52 ± 0.33 (0.79)	≥ 0.25
Photon index	2.0	1.9 (2.0)	$2.0^{+4}_{-0.6}$
N_H ($\times 10^{22}$ cm^{-2})	2.9 ± 0.4	2.9 ± 0.3	3–20
Central E (keV): Mg XI	1.336 ± 0.010	1.328 ± 0.020	...
Si XIII	1.843 ± 0.009	1.828 ± 0.020	...
S XV	2.450 ± 0.040	2.426 ± 0.018	...
Equivalent width (eV): Mg XI	475	136 (398)	...
Si XIII	409	163 (291)	...
S XV	157	359 (344)	...

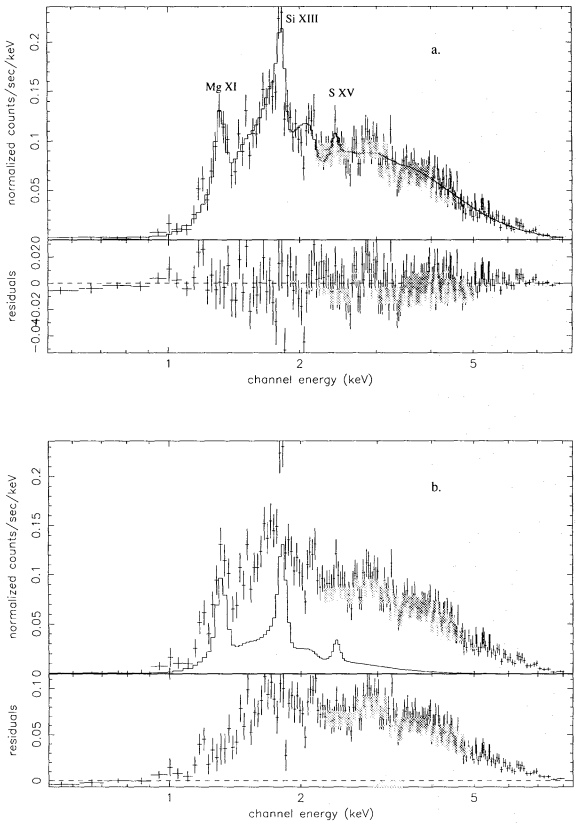

FIG. 5.—(*a*) Same spectrum as in Fig. 4*a* but fitted with a model including a power-law component (fixed with $\Gamma = 2.0$), thermal bremsstrahlung emission, interstellar absorption, and Gaussian fits to the three most prominent emission lines. (*b*) Spectrum fitted with the same model as in (*a*), but with the power-law component omitted. The best-fitting values are listed in Table 2.

energies ≤ 1 keV, we cannot see either the low-energy emission lines of O and Ne expected for a Type II supernova or the bright Fe L complex expected for a Type Ia supernova. However, the strong Mg line is consistent with G29.7−0.3 being the remnant of a Type II supernova.

4. DISCUSSION

Using 21 cm observations, Becker & Helfand (1984) determined a kinematic distance to G29.7−0.3 of 19 kpc with an uncertainty of a few kiloparsecs. This, taken with the angular size of the shell of 1′.75, gives a shell radius of 9.7 pc. Using this information combined with the temperature and column density that we obtained from the spectral analysis of the *ASCA* data, we compute here the luminosity of the Crab-like and shell components, the mass of the remnant, and its age.

4.1. *Luminosity*

Using XSPEC, we determined the flux of the Raymond-Smith thermal plasma component in the range 0.5–8 keV using the temperature and column density derived from a simultaneous fit to the observations with the two SIS detectors. The flux from this portion of the spectrum corresponds to the emission from the shell component. The fit gives a value of $2.3^{+0.1}_{-0.6} \times 10^{-12}$ ergs cm^{-2} s^{-1}.

To calculate the luminosity of the Crab-like component, we measured the flux in the range 0.5–8 keV due to a power-law distribution with $\Gamma = 2.0$ and the normalization we derived from the spectral fit. We include the interstellar absorption as above. From this, we measure a flux of $(2.2 \pm 0.1) \times 10^{-11}$ ergs cm^{-2} s^{-1}.

Assuming a distance of 19 kpc, the luminosities of the two components are $L_{\rm shell} = 1.0 \times 10^{35}$ ergs s^{-1} and $L_{\rm core} = 9.6 \times 10^{35}$ergs s^{-1}. Note that the X-ray luminosity of the core given by Becker & Helfand (1984) of 4×10^{36} ergs s^{-1} resulted from a computational error; using the observed *Einstein* flux and correcting this error give $L_{\rm core} = 1.2 \times 10^{36}$ ergs s^{-1}, close to the value we obtain. The Crab-like component of G29.7−0.3 is still more luminous in X-rays than any other Galactic Crab-like SNR or Crab-like component of a composite SNR excepting only the Crab itself (Helfand & Becker 1987).

4.2. *Mass*

We compare the measured luminosity of the shell component to the luminosity of an analytical model of gas at the temperature derived from the SIS and filling a volume the size of the SNR. The analytical luminosity is given by the cooling function for a Raymond-Smith plasma multiplied by the volume of the remnant: $L_{\rm X} = \Lambda_{\rm RS} V$, where $V = 4\pi R^3/3$ (filled-sphere geometry) or $V = \pi R^3/3$ (thin-shell geometry with $dR = R/12$) and $\Lambda_{\rm RS} = C_{\rm RS} n_e n_{\rm H}$ (Raymond, Cox, & Smith 1976), where we let $n_e n_{\rm H} = n_{\rm H}^2$. From our observations, $kT = 0.50$ keV and the corresponding cooling function in the 0.5–8.0 keV band is $C \approx 2 \times 10^{-23}$ ergs cm^{3}s^{-1}. In order for $L_{\rm X}$(meas) = $L_{\rm X}$(anal), we require $n_{\rm H} = 0.21$ cm^{-3} (filled-sphere geometry) or $n_{\rm H} = 0.42$ cm^{-3} (thin-shell geometry). This number density, the SNR's radius of 9.7 pc, and approximating the composition to be hydrogen, give a total mass of 10 (shell) or 20 (sphere) $M_\odot$ for the hot gas in G29.7−0.3. The evidence for a compact object at the center of G29.7−0.3 and the elements seen in the ejecta indicate that the SNR's progenitor was a massive star. Therefore, the total mass we estimate is probably largely composed of the material ejected from the parent star and includes relatively little swept-up interstellar material, suggesting that the remnant is nearly freely expanding into a low-density medium. Highly enriched abundances and the expected nonequilibrium ionization could decrease these mass estimates by up to a factor of ~ 2 (Hughes & Singh 1994).

4.3. *Age*

If the SNR is in its free-expansion phase with $v_{\rm exp} \approx 10^4$ (or 5×10^3) km s^{-1}, its radius of 9.7 pc implies an age of $\approx$900(1800) yr. If it is not freely expanding, its age may be closer to that derived from the Sedov relations, in which

$$R \approx 13 \left(\frac{E_{51}}{n_0}\right)^{1/5} t_4^{2/5} \text{ pc} , \quad (1)$$

where E is the explosion energy in units of 10^{51} ergs and t_4 is the age in units of 10^4 yr; in this case the shock temperature is

$$T \approx 0.45 \left(\frac{E_{51}}{n_0}\right)^{2/5} t_4^{-6/5} \text{ keV} . \quad (2)$$

Combining these equations and solving for t_4 yield

$$t_4 \approx \frac{R}{13} \left(\frac{0.45}{T}\right)^{1/2} . \quad (3)$$

Using $R = 9.7$ pc and $kT = 0.50$ keV, we determine the age to be ≈ 7000 yr. The shock temperature, however, may well be higher than our measured temperature, suggesting that this age estimate may be too high. In addition, since the remnant has a small total mass, it is probably closer to the free-expansion age; thus, 900 yr $< t \ll 7000$ yr.

Using measurements from known pulsars, Seward & Wang (1988) find that the 0.2–4 keV band X-ray luminosity (including emission from the compact source and synchrotron nebula) is related to a pulsar's rate of rotational energy loss by the following equation:

$$\log L_X = 1.39 \log \dot{E} - 16.6 . \quad (4)$$

For G29.7−0.3, we measure $L_X = 3.9 \times 10^{35}$ ergs s^{-1} in the 0.2–4 keV energy range, which translates to an $\dot{E} = 3.5 \times 10^{37}$ ergs s^{-1}. Under the assumptions that a pulsar's true age is equal to its characteristic age ($= P/2\dot{P}$) and its moment of inertia, $I = 10^{45}$g cm^2, Seward & Wang (1988) find the period,

$$P = 0.25[t(10^3 \text{ yr})]^{-1/2}[\dot{E}(10^{37} \text{ ergs s}^{-1})]^{-1/2} \text{ s} , \quad (5)$$

the period derivative,

$$\dot{P} = 1.58 \times 10^{-11}[P(\text{s})][t(10^3 \text{ yr})]^{-1} \text{ s s}^{-1} , \quad (6)$$

and the surface magnetic field,

$$B_0 = [P(\text{s})\dot{P}(10^{-15} \text{ s s}^{-1})]^{1/2} \times 10^{12} \text{ G} . \quad (7)$$

This approximation works well for the Crab pulsar even though its period is only approximately twice its initial period.

We have three equations and four unknowns, so we may proceed in different ways. If we assume a magnetic field similar to that of the Crab pulsar ($B_0 = 5 \times 10^{12}$ G) and include our measured value for $\dot{E}$, we predict that the pulsar in G29.7−0.3 has a period $P = 0.073$ s, a period derivative $\dot{P} = 350 \times 10^{-15}$ s s^{-1}, and an age $t = 3300$ yr. On the other hand, if we assume an age closer to the age derived above from the size and mass of the remnant ($t \approx 10^3$ yr), we find $P = 0.133$ s, $\dot{P} = 2100 \times 10^{-15}$ s s^{-1} and $B_0 = 16.7 \times 10^{12}$ G. This second set of characteristics is very similar to those measured directly for the young pulsar PSR 1509−58 (Seward & Wang 1988) which is also embedded in a shell-type remnant: $\dot{E} = 1.8 \times 10^{37}$ ergs s^{-1}, $P = 0.150$ s, $\dot{P} = 1540 \times 10^{-15}$ s s^{-1}, and $B_0 = 15 \times 10^{12}$ G.

With their VLA observations of G29.7−0.3, Becker & Helfand (1984) measured a flux for the core component of 0.275 Jy at 6 cm and a spectral index of $\alpha_r = 0.0$ between 2 and 20 cm. Combining this with our measured flux density of 1.21 μJy at 4 keV and a spectral index of $\alpha_X = 1.0$, we derive a break frequency in the synchrotron nebula's spectrum of $\nu_b \approx 10^{13}$ Hz (the same as that for the Crab), implying a young age for the SNR. We can estimate the nebular magnetic field by using the following expression for the energy density of relativistic electrons:

$$U_e = B^{-3/2}\left[\epsilon_\nu \frac{mc^2}{1-2\alpha_r}\left(\frac{2\pi mc}{e}\right)^{1/2-\alpha_r}\frac{\nu_b^{1/2-\alpha_r}}{1.7\times 10^{-21}a(p_r)} \times \left(\frac{\nu_b}{4\times 10^6}\right)^{\alpha_r} + \epsilon_\nu \frac{mc^2}{1-2\alpha_X}\left(\frac{2\pi mc}{e}\right)^{1/2-\alpha_X} \times \frac{\nu_b^{1/2-\alpha_X}}{1.7\times 10^{-21}a(p_X)}\left(\frac{\nu_b}{4\times 10^6}\right)^{\alpha_X}\right] , \quad (8)$$

where $\epsilon_\nu = 3.6 \times 10^{-34}$ ergs s^{-1} cm^{-3} Hz^{-1} is the flux density of the synchrotron nebula at the break frequency and a is a constant that depends on the cycloid particle energy index, $p(=2\alpha+1)$. Invoking equipartition, $U_e = (4/3)U_B = B^2/6\pi$, we find a nebular magnetic field of $B = 1.8 \times 10^{-4}$ G. This, in turn, gives a total energy for the magnetic field and the relativistic particles of $E = 9.9 \times 10^{47}$ ergs. Using values derived directly from the radio and X-ray observations, then, we estimate the remnant age as $t = E/\dot{E} \approx 900$ yr, consistent with the free-expansion approximation.

5. CONCLUSIONS

We confirm the composite nature of the supernova remnant G29.7−0.3 by demonstrating the existence in its *ASCA* spectrum of spatially distinct thermal and nonthermal components. The power-law component from a central synchrotron nebula dominates at high energies, and its photon index is similar to that of the Crab. Its X-ray luminosity suggests it is powered by a young pulsar with a spin-down energy of 3.5×10^{37} ergs s^{-1}. The thermal shell shows prominent lines of Mg, Si, and S, characteristic of the spectrum expected from the ejecta of a massive progenitor. We estimate a mass of 10–20 $M_\odot$ for the supernova remnant, including mass ejected by the star and swept up in the interstellar medium, suggesting that the remnant is still freely expanding. The shell luminosity and diameter suggest an age for the remnant of $\approx 10^3$ yr; the energetics of the central synchrotron nebula are consistent with this estimate. Further observations with higher resolution instruments (such as *AXAF*) will help to define better the abundances and temperature distribution in the shell, providing a more precise determination of the age and progenitor mass for this prototypical composite supernova remnant.

This work was supported at Columbia University under grant NAG 5-2556 from the NASA *ASCA* Guest Observer program, and has made use of data from HEASARC. This is Contribution 590 of the Columbia Astrophysics Laboratory.

REFERENCES

ABC Guide to *ASCA* Data Reduction. 1994, available from the *ASCA* Guest Observer Facility, Office of Guest Investigator Programs, Laboratory of High Energy Astrophysics (Greenbelt: NASA GSFC)
Becker, R. H., & Helfand, D. J. 1984, ApJ, 283, 154
Becker, R. H., Helfand, D. J., & Szymkowiak, A. E. 1983, ApJ, 268, L93
Fierro, J. M., et al. 1995, ApJ, 447, 807
Green, D. A. 1995, A Catalogue of Supernova Remnants (Cambridge: Mullard Radio Astronomy Obs.)
Helfand, D. J. 1993, unpublished
Helfand, D. J., & Becker, R. H. 1987, ApJ, 314, 203
Hughes, J. P., & Singh, K. P. 1994, ApJ, 422, 126
Raymond, J. C., Cox, D. P., & Smith, B. W. 1976, ApJ, 204, 290
Raymond, J. C., & Smith, B. W. 1977, ApJS, 35, 419
Seward, F. D., & Wang, Z. 1988, ApJ, 332, 199
Tammann, G. A., Loeffler, W., & Schroeder, A. 1994, ApJS, 92, 487
Tanaka, Y., Inoue, H., & Holt, S. S. 1994, PASJ, 46, L37
Vasisht, G., Kulkarni, S. R., Aoki, T., Dotani, T., & Nagase, F. 1995, preprint
Warwick, R. S., Norton, A. J., Turner, M. J. L., Watson, M. G., & Willingale, R. 1988, MNRAS, 232, 551
Warwick, R. S., Turner, M. J. L., Watson, M. G., & Willingale, R. 1985, Nature, 317, 218
Yamauchi, S., & Koyama, K. 1993, ApJ, 404, 620